



climate change initiative

European Space Agency

Product Validation and Intercomparison Report (PVIR)



glaciers
cci

Prepared by: Glaciers_cci consortium
Contract: 4000127593/19/I-NB
Name: Glaciers_cci+D4.1_PVIR
Version: 1.1
Date: 21.12. 2021

Contact:
Frank Paul
Department of Geography
University of Zurich
frank.paul@geo.uzh.ch

Technical Officer:
Anna Maria Trofaier
ESA Climate Office



UNIVERSITY
OF OSLO



University of
Zurich^{UZH}



UNIVERSITY OF LEEDS

 **GAMMA REMOTE SENSING**

 **enveo**

Document status sheet

Version	Date	Changes	Approval
1.0	10.11. 2021	Consolidated first draft	J. Wuite
1.1	21.12. 2021	Finalized first version	F. Paul

The work described in this report was done under ESA contract 4000127593/19/I-NB. Responsibility for the contents resides with the authors who prepared it.

Author team:

Jan Wuite, Thomas Nagler, Ludivine Libert (ENVEO), Frank Paul, Philipp Rastner (GIUZ), Tazio Strozzi, Andreas Wiesmann (Gamma), Andreas Kääb, Désirée Treichler, Livia Piermattei (GUIO), Lin Gilbert, Andrew Shepherd (SEEL).

Glaciers_cci Technical Officer at ESA:

Anna Maria Trofaier

Table of Contents

1. Introduction	4
1.1 Purpose and Scope	4
1.2 Document Structure	4
1.3 Related Documents	4
2. Use Case I (Eastern Arctic)	5
2.1 Introduction.....	5
2.2 Validation and Intercomparison	5
2.2.1 Area uncertainty (Franz-Josef-Land)	5
2.2.2 Velocity from SAR.....	5
2.2.3 Elevation Change from Altimetry	13
3. Use Case II (HMA)	16
3.1 Introduction.....	16
3.2 Validation and Intercomparison	16
3.2.1 Length changes and advance rates	16
3.2.2 Velocity from optical and SAR	16
3.2.3 Elevation change	25
4. References	30
Acronyms	32

1. Introduction

1.1 Purpose and Scope

This document is the Product Validation and Intercomparison Report (PVIR) for the ESA Glaciers CCI+ project. The PVIR describes the validation and cross comparison activities of the parameters that are under development in the project, including: validation data, study sites and validation results. The validation and quality assessment methodology are described in detail in the Product Validation Plan (PVP; [RD1]). The validation results presented here focuses on the two use cases: I) Eastern Arctic, and II) High Mountain Asia (HMA). The geophysical parameters and corresponding data products on glaciers in these regions are: 1) length changes and change rates, 2) ice velocity, and 3) elevation change.

1.2 Document Structure

This document is structured into an introductory chapter followed by two chapters focussed on the validation and product intercomparison for each of the two use cases:

- Use Case I (Eastern Arctic)
- Use Case II (HMA)

Both chapters provide a short introduction followed by an overview of the validation and product intercomparison datasets and results. The last chapter provides a list of the references.

1.3 Related Documents

Acronym	Title	Document reference	Version	Date
[RD1]	Product Validation Plan	Glaciers_cci+D1.3-2_PVP	2.1	10.10.2021
[RD2]	Climate Research Data Package	Glaciers_cci+D3.2_CRDPv2	1.0	08.10.2021

2. Use Case I (Eastern Arctic)

2.1 Introduction

This section describes the accuracy assessment and validation of products generated for Use Case 1 (Eastern Arctic). The products include glacier outlines derived from optical satellite sensors, ice velocity maps, time series of glacier velocity derived from contemporary and historic Synthetic Aperture Radar (SAR) missions and elevation changes derived from a suite of radar altimetry missions. The products cover a large territory with glacierized archipelagos in the Eastern Arctic, including Novaya Zemlya, Franz-Josef-Land, Severnaya Zemlya and Svalbard. The datasets contribute to fundamental climate data records (FCDRs) over time periods ranging from days to decades.

2.2 Validation and Intercomparison

2.2.1 Area uncertainty (Franz-Josef-Land)

Glacier outlines have been derived from several Sentinel-2 tiles mostly acquired on 12.09.2016 with the standard band ratio method (red/SWIR) and an additional threshold in the blue band to remove wrongly classified ocean water. As the ice caps were largely debris free and sea ice was not present, the automatically derived glacier outlines had only locally to be corrected, mostly in regions with cloud cover. Due to the limited manual corrections, uncertainty was estimated with the buffer method, assuming a ± 10 m (1 pixel) uncertainty of the glacier perimeter. This resulted in a $\pm 2.7\%$ uncertainty of the area or 12264 ± 331 km².

We also mapped glacier extents in 1962 using declassified images from the Corona KH4 sensor. These were acquired 54 years earlier on 18.9.1962 and orthorectified with the ArcticDEM using 8 to 42 GCPs for each of the image-stripes. After merging to a mosaic, outlines were created using a threshold value to eliminate dark ocean water and a 2 km buffer on RGI6 glacier extents to remove most of the sea ice. Afterwards, all raw outlines were checked against the Corona image mosaic (which is black and white) and the respective Sentinel-2 tiles (false colour composite) and corrected by manual on-screen digitizing. The key challenge here was that all stripes had a thin snow cover also outside of glaciers and the interpretation was largely guided by subtle changes in contrast. To improve certainty, a first interpretation by one analyst was cross-checked by a second analyst. For individual glaciers we found large differences in interpretation, partly exceeding 100% of the original glacier area, but most differences were in the 5-20% range. Most glacier extents were digitised too large by the first analyst, but some snow-covered ice caps were missed. In view of the large total area covered and only considering our rule-set for interpretation, the overall uncertainty of the final dataset is estimated to be smaller than 5%.

2.2.2 Velocity from SAR

In the course of the project, several ice velocity (IV) products have been generated for various regions and time frames using different techniques and sensors. In this section, we validate the following products, targeting the Eastern Arctic and already listed in [RD2]:

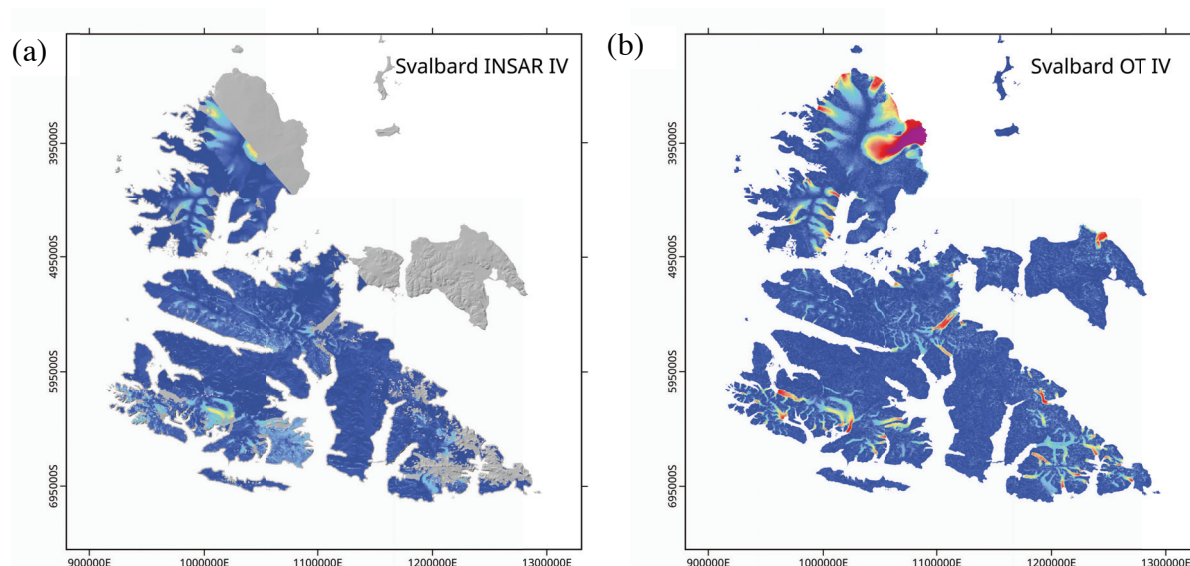
- Svalbard ice velocity from Sentinel-1 SAR interferometry (winter 2018-2019)
- Ice velocity maps from historical SAR data covering the Eastern Arctic
- Ice velocities computed from offset-tracking of Sentinel-1 data over the Eastern Arctic

2.2.2.1 Svalbard Sentinel-1 InSAR Ice Velocity

For intercomparison and validation of the Sentinel-1 (S-1) interferometric (InSAR) IV map of Svalbard, we select the two following quality assessment (QA) methods, that are described in [RD1]:

- (1) QA-IV-3: Stable area test
- (2) QA-IV-5: Intercomparison with IV products from different sources

The intercomparison (2) is conducted against the S-1 offset tracking (OT) IV product with 250 m pixel size (2016-2019). As the S-1 InSAR map has a 50 m pixel size, the offset-tracking product is up-sampled to match this resolution. The comparison is performed over glacierized areas only, using a glacier mask derived from RGI 5.0. In Figure 2.1 we present the InSAR and OT IV maps used for the comparison, as well as the classification of Svalbard between glaciers and stable terrain. The stable terrain shown in this figure is derived from the Svalbard outline from which the glacier mask has been subtracted. It used hereafter for the stable area test.



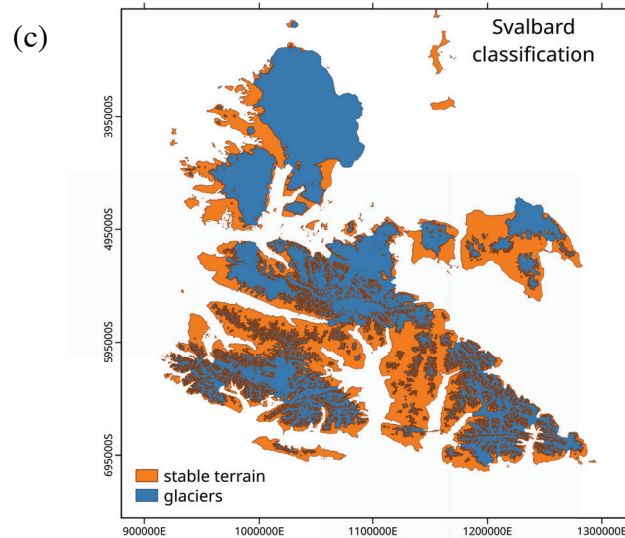


Figure 2.1: (a) Svalbard Sentinel-1 interferometric IV map from crossing orbits (winter 2018-2019). (b) Svalbard Sentinel-1 offset-tracking IV map (2016-2019). (c) Svalbard classification of stable terrain and glaciers, based on RGI 5.0.

QA-IV-3: Stable area test

For the stable terrain analysis, the interferometric IV map is masked using the stable terrain mask shown in Figure 2.1c and histograms of the velocity distribution are computed for the x- and y-components (i.e. East and North) and for the velocity magnitude. In Figure 2.2 the statistical measures associated to the velocity distribution are displayed along with the histograms. The minimum, maximum, mean, standard deviations, median and RSME values are provided. Over stable terrain, we expect null velocity. We observe that for each component, the distribution is slightly shifted with respect to the zero velocity. The mean and median values of the distribution indicate deviations by about 1 cm d^{-1} , with standard deviations of the same order. The RSME values, calculated as the measurement deviations from the zero velocity, reach 1.4 to 2 cm d^{-1} . Since these values are larger than the standard deviation, it suggests that the velocity measurements are slightly biased.

The deviation from the zero velocity values over stable terrain is most likely due to the phase unwrapping areas that are observed in InSAR IV map and that shift the velocity estimates over large regions. Artifacts likely caused by topography are also observed in the interferometric velocity measurements.

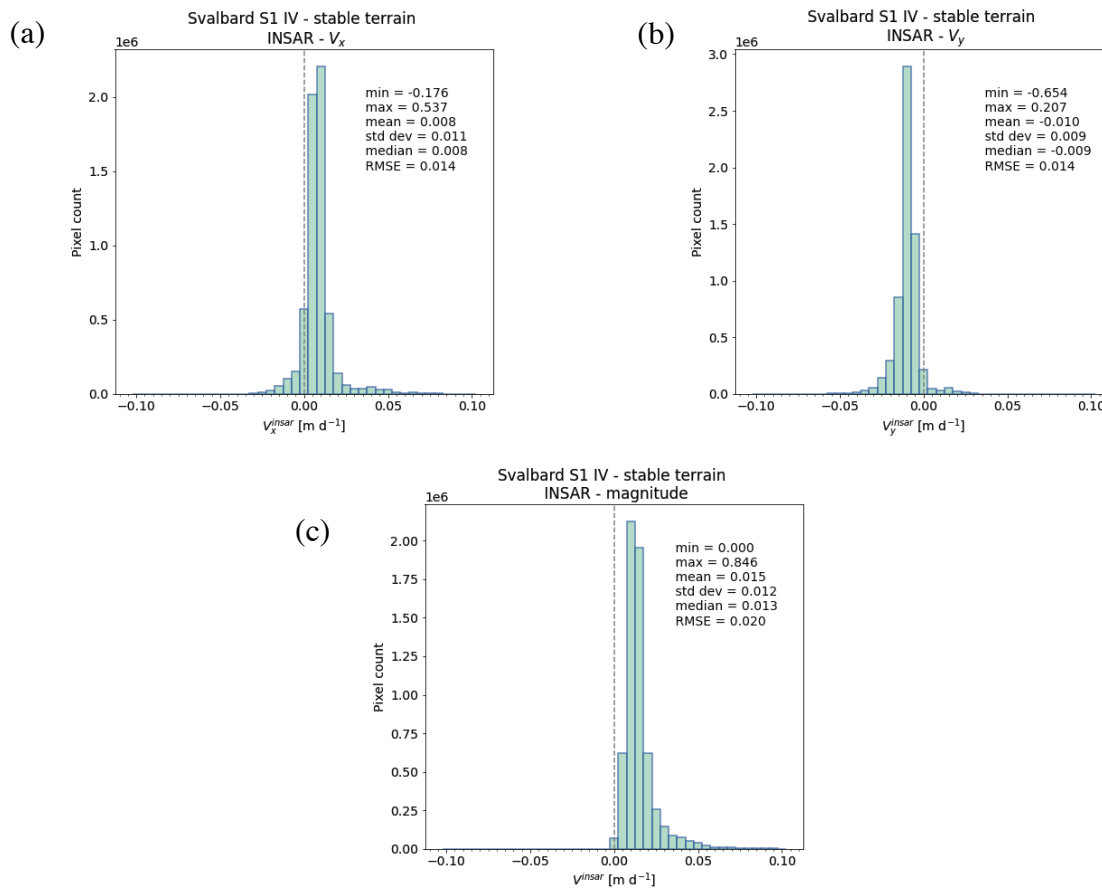


Figure 2.2: Histograms of Svalbard Sentinel-1 interferometric ice velocity map over stable terrain. (a) V_x . (b) V_y . (c) velocity magnitude. Each histogram is annotated with the minimum, maximum, mean, standard deviation, median and RSME values of the distribution.

QA-IV-5: Intercomparison with IV products from different sources

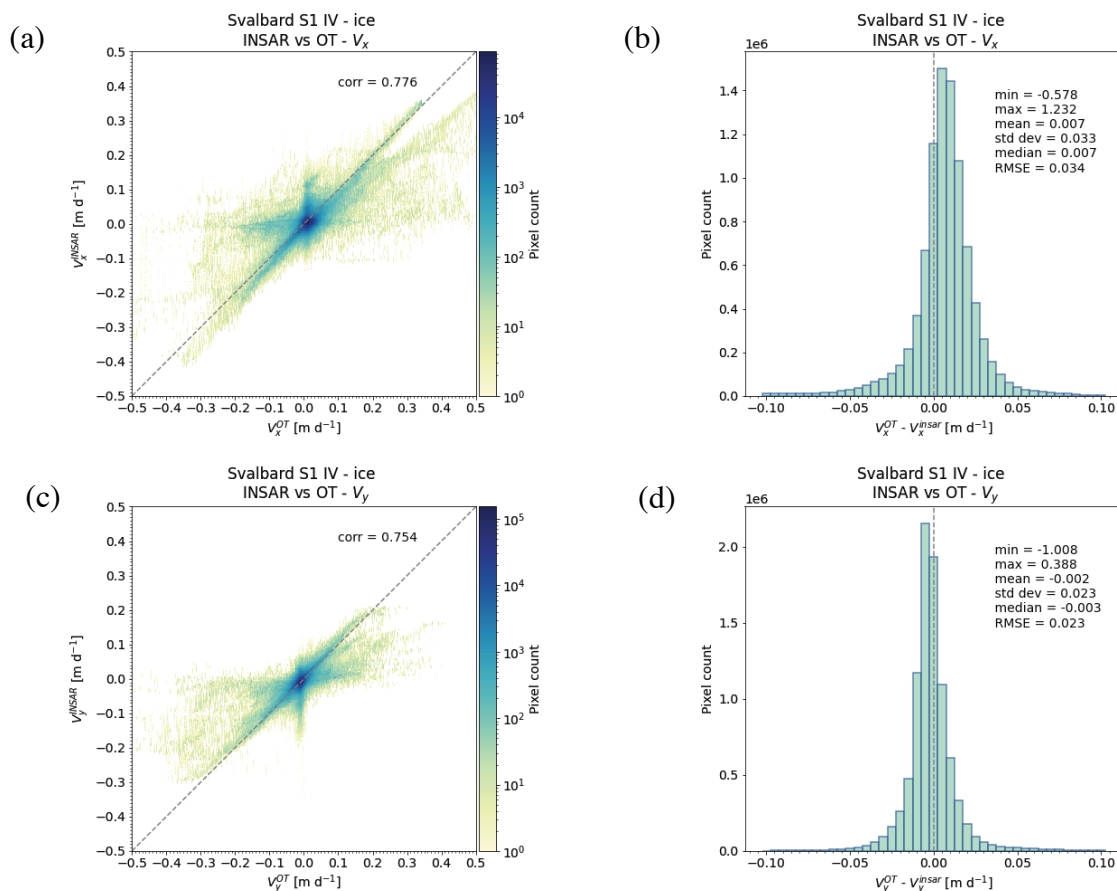
The Sentinel-1 InSAR IV map is compared here with a Sentinel-1 IV map generated with offset-tracking. While the InSAR map is generated from acquisitions spanning the winter season of 2018-2019, the OT one is derived from data acquired between 2016 and 2019. The coverage of the InSAR is also less than the one captured by offset-tracking, because (1) crossing orbits are not covering the whole area, and (2) regions of decorrelated signal, due e.g. to fast-flow, are masked out.

For comparing InSAR and OT IV products, we compute (1) scatter plots of the InSAR velocity component against the OT velocity component, color-coded in terms of pixel density, and (2) histograms of the difference between the OT and IV components. The scatter plots and histograms are calculated for the x- and y-velocity components, as well as for the velocity magnitude (Figure 2.3).

The scatter plot represents the correlation between both parameters. As they represent the same quantity, but measured in a different way, the points are expected to be around the 1:1 line and to have a correlation coefficient close to 1. For all three components, we can observe an overlap of different trends: a main one close to identity line but slightly tilted, overlaid with an almost-horizontal and an almost-vertical trend. The finer details in the InSAR map

may be the reason of the horizontal trend: because InSAR is less affected by noise and it better resolves the shear margins than OT, a given pixel may have a small value in the InSAR products while its value will be higher in the OT product. Some points may deviate from the main trends, especially for velocities larger than 1 cm d^{-1} . Such points are likely associated to phase unwrapping errors in the InSAR product. Points with smaller velocity values are densely gathered around the origin. The correlation coefficient only reaches values about 0.75, indicating a moderate agreement between both products.

The histograms shown in Figure 2.3 are computed from the pixel-by-pixel difference of InSAR and OT products. In case of a good agreement between both products, the distribution is expected to be centred around zero, and to show as little spread as possible. While the distribution of the x-component (east) shows discrepancies in the order of 1 cm d^{-1} on average, the y-component show differences around 0.3 cm d^{-1} , but with the opposite sign. This indicates that both products have a slight difference in the orientation of their flowlines. Rotation of the flowlines of one product with respect to the other also explains the tilt observed in the main trend of the scatter plots. The histogram of the velocity magnitude also shows some deviations of a few millimetres per day from the null central trend. For all three components, the RMSE and standard deviations values range around $2\text{-}3 \text{ cm d}^{-1}$. Both scatter plots and histograms exhibit a moderate agreement between InSAR and OT products, thus indicating that errors contained in the S-1 InSAR IV map might be significant in places.



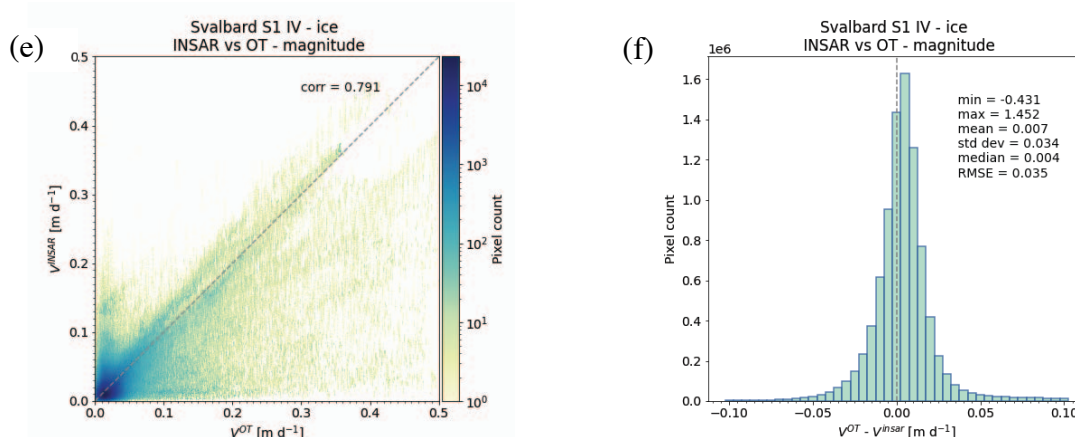


Figure 2.3: Intercomparison of interferometric and offset-tracking ice velocity products over Svalbard glaciers. Scatter plots of interferometric IV against OT IV are shown in the left column, with the correlation coefficient annotated. Histograms of the velocity differences are shown in the right column, along with the minimum, maximum, mean, standard deviation, median and RSME of the distribution. (a)-(b) V_x . (c)-(d) V_y . (e)-(f) velocity magnitude.

2.2.2.2 Historical SAR data

Nearly complete mosaics of winter ice surface velocities for the 1990's over the Eastern Arctic (Novaya Zemlya, Franz-Josef-Land, Severnaya Zemlya and Svalbard) were compiled based on historical SAR data. Offset-tracking to JERS-1 SAR data of the time period 1992-1998 was mainly applied. Data gaps were complemented using SAR interferometry and offset-tracking of ERS-1/2 SAR data of the time period 1991-1997. In order to study long-term variability of winter ice surface velocity, velocity maps were also computed with offset-tracking from 2008-2011 ALOS-1 PALSAR-1 data.

The velocities derived from offset-tracking of JERS-1 (1992-1998) and ERS-1/2 (1991-1997) data are available in vector format with metadata information for single image tracks. A comma-separated values (csv) file provides the northing and easting coordinates of measurement points, the elevation, the displacement in metres in the x, y and z directions, and the cross-correlation coefficient for each measurement. A metadata file in xml format provides information about the SAR images used, the processing parameters and quality aspects of the data such as the percent of valid information over ice and statistical measures over ice-free regions. According to previous studies, the SAR-derived velocities have uncertainties of ± 20 m/a for JERS-1 (Strozzi et al., 2008), ± 40 m/a for ERS-1 (Dowdeswell et al., 2008) and ± 10 m/a for ALOS-1 PALSAR-1 (Paul et al., 2015).

The ERS-1/2 InSAR ice velocity map of Nordaustlandet (Svalbard) combines interferometric phases from 1-day ERS-1/2 image pairs and is produced for the winter 1995/1996 at 100 m resolution. Method and uncertainties are described in Dowdeswell et al. (2008). In most cases errors are assumed to be smaller than 7 m/a, while for unfavourable combinations of image pairs this value is slightly larger. The ERS-1/2 InSAR ice velocity map of south Svalbard is produced from winter 1996 and 1997 data at 20 m resolution. Method and uncertainties are described in Nuth et al. (2019). The accuracy was measured by extracting displacements across a point grid of 1000 m spacing excluding points which were not on stable terrain (glaciers, fjords, etc.). Nuth et al. (2019) found a median value of 2.3 m/a and a standard deviation



of 2.6 m/a. The same processing and accuracy assessment procedure was also applied to 1-day ERS-1/2 image pairs of winter 1995/1996 over north-west Svalbard. In this case, a median value of 4.0 m/a and a standard deviation of 3.7 m/a were found.

2.2.2.3 Sentinel-1

Ice surface velocities computed from offset-tracking of S-1 data over the Eastern Arctic have been validated in the previous phase of the project by means of SAR data at higher spatial resolution (Radarsat-2 Wide Ultra Fine) and ground-based radar measurements (Strozzi et al., 2017). The overall uncertainty of the ice surface velocity products derived from S-1 data with a time interval of 12 days estimated from the inter-comparison exercises in areas far from relatively small glacier's calving fronts and shear zones is between ± 20 and ± 30 m/a (± 0.05 to ± 0.08 m/d). These numbers correspond well to the statistical measures of ice surface velocity that are computed for every individual S-1 frame over ice-free regions. In addition, by assuming a precision of 1/20th of a pixel in the offset estimation, the displacement error of S-1 interferometric wide (IW) swath data with pixel sizes in ground-range and azimuth direction of $8 \text{ m} \times 20 \text{ m}$, respectively, and a time interval of 12 days is also on the order of 30 m/a.

For this phase of project, we specifically focus on surging glaciers, i.e. glaciers characterized by rapid temporal and spatial changes of velocity. For this reason, we used as far as possible every single image pair that is computed and expand our investigations to narrow glaciers and in areas close to calving fronts and shear zones. Aggregation of results over time periods of months or years to improve the quality of the results cannot be obviously accomplished for these studies as the surface of surging glaciers is destroyed and cannot be tracked over more than just a few days to weeks. Quality aspects of the data such as the percent of valid information over ice and statistical measures over ice-free regions, which are computed for every SAR image pair of the same tracks and frames and are indeed useful to generally indicate the adequacy of the results on a regional scale (Figure 2.4), cannot be considered to specifically evaluate the usefulness for an individual glacier.

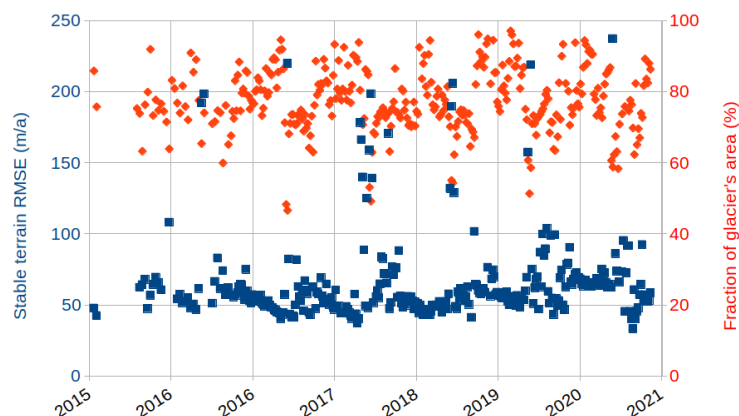


Figure 2.4: Time-series of Sentinel-1 data over Spitsbergen (Svalbard): statistical measures over ice-free regions (left axis) and coverage of valid measurements for the glacier area (right axis). In general, the quality of summer data, both in terms of stable terrain RMSE and fraction of glacier's area, is lower than that of winter data.

Additionally, the high temporal variability of IV over surging glaciers makes the sensor inter-comparison very challenging if the dates are not coincident. As an example, we show in Fig-

ure 2.5 the time-series of S-1 and Sentinel-2 (S-2) velocity for one point over Negribreen (Svalbard). Temporal changes of velocity are very prominent, in particular during the summer when short speed-up events are superimposed on the general surging cycle. The intercomparison of S-1 and S-2 IV clearly shows that even if data are only a few days apart they cannot be used for validation. GPS data would be ideal for a proper validation, but they are not available to us and in general very hard to realize on fast-flowing surging glaciers.

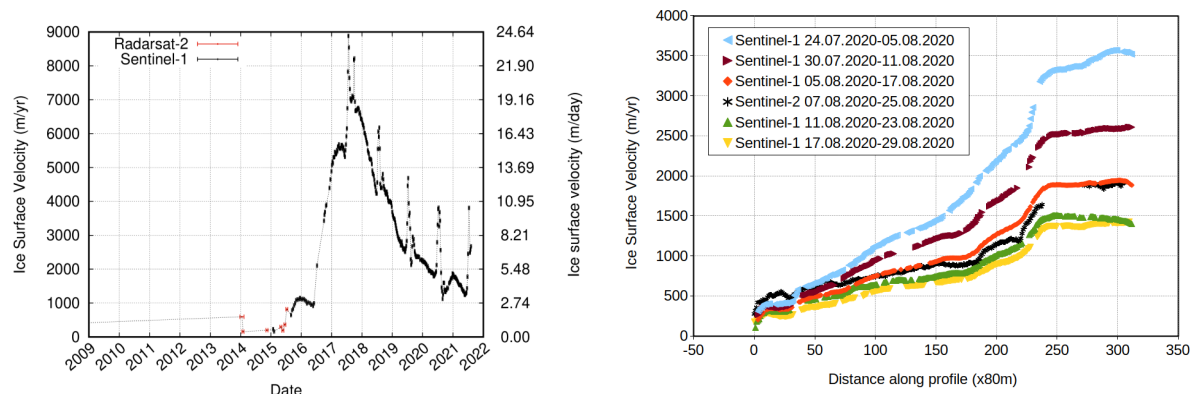


Figure 2.5: Left: Time-series of Sentinel-1 data over Negribreen. Right: Ice surface velocity on a profile along the centre flow-line of Negribreen from Sentinel-1 and Sentinel-2 data.

Sensor intercomparison is nevertheless essential to highlight limitations and adjust tracking parameters. The results over the surging Scheelebreen (Svalbard) are illustrative for this point (Figure 2.6). The automatic processing chain set-up at Gamma for the continuous, automatic processing of S-1 data over the Eastern Arctic uses a template size of 512x128 pixels and a time interval of 12 days. This results in a strong underestimation of the motion of Scheelebreen at the peak of its surge in the summer of 2021, because of the relatively narrow glacier (width of about 1 km) and of strong changes at the surface of the glacier as a result of the surge and of melting ice and snow. Adjustment of the tracking parameters to a template size of 320x64 pixels and a time interval of 6 days resulted in much better results towards the end of the summer, when the changes at the surface of the glaciers were more limited. Results from different sensors can eventually be integrated for a more complete study of a surge (Figure 2.7).

In conclusion, the uncertainty of Sentinel-1 ice surface velocity data over surging glaciers is temporally and spatially highly variable. It is thus very challenging to determine it quantitatively.

SAR backscatter changes over time (Leclercq et al. 2021) indicate well where glacier surfaces become highly crevassed and thus indicate surges well. Similarly, animation of repeat S-1 data is typically well suited to visualize a surge, even if velocity measurements fail. Both methods provide no quantitative measurements of ice flow. Still, they provide a valuable qualitative validation of velocity measurements by confirming an ongoing surge and also giving an indication of the magnitude of ice flow speeds and severity of surface changes, or by indicating where and why velocity measurements are expected to fail.

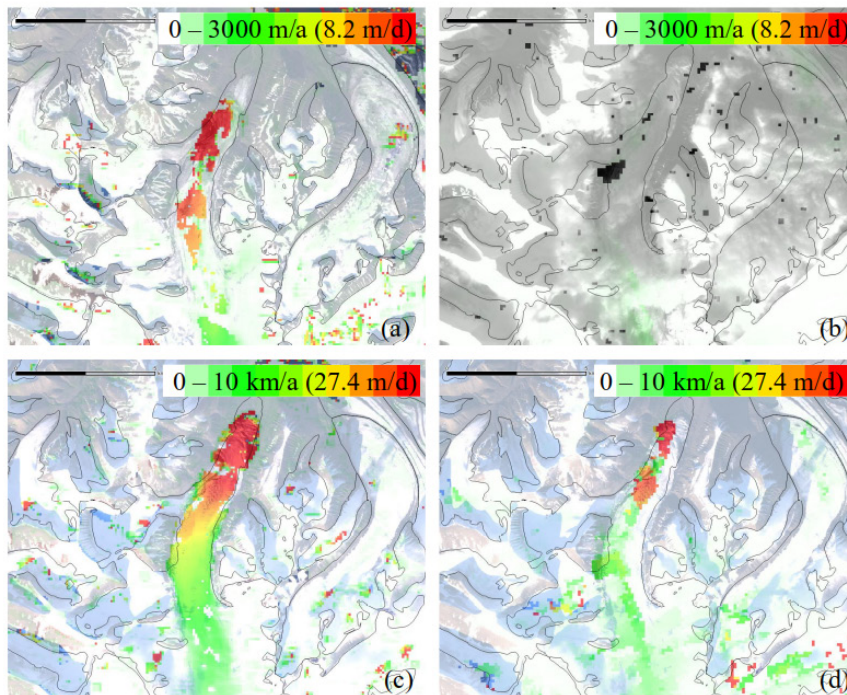


Figure 2.6: Ice surface velocity of Scheelebreen (Svalbard) from Sentinel-1 and Sentinel-2 data: (a) Sentinel-2 26.07.2021-08.08.2021, (b) Sentinel-1 18.08.2021-30.08.2021 with image template size of 512x128 pixels, (c) Sentinel-2 11.09.2021-13.09.2021, (d) Sentinel-1 11.09.2021-27.09.2021 with image template size of 320x64 pixels.

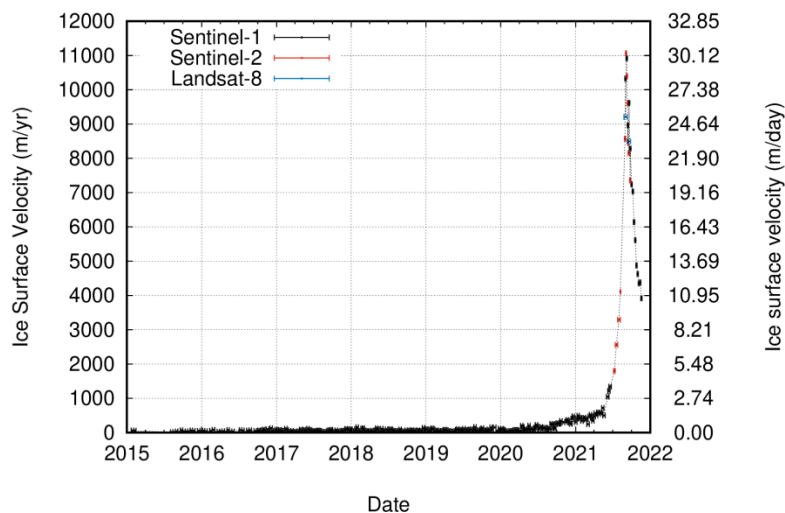


Figure 2.7: Time-series of ice surface velocity from Sentinel-1, Sentinel-2 and Landsat-8 over Scheelebreen (Svalbard).

2.2.3 Elevation Change from Altimetry

The input datasets assembled for the Eastern Arctic use case come from six radar altimetry missions. The sensors, in order of launch date, are ERS-1/2 Radar Altimeter (RA), EnviSat RA-2, CryoSat-2 SAR Interferometric Radar Altimeter (SIRAL), and Sentinel-3A/B SAR Altimeter (SRAL). CryoSat-2 SIRAL can operate in more than one mode, but over the East Arctic only SARIn (SAR Interferometry mode) is used.

Accuracy is assessed by comparing measured elevations against independent validation data, which has been performed for ERS-2 and Envisat against the ICESat laser altimeter (Brenner et al, 2007), for CryoSat-2 against the NASA IceBridge Airborne Topographic Mapper (ATM) (Nilsson et al, 2016) and for Sentinel-3A against the NASA IceBridge ATM and Riegl Laser Altimeter (RLA) (McMillan et al, 2019). The performance of ERS1 should be similar to that of ERS2, and of Sentinel-3B to Sentinel-3A. Table 2.1 below summarises the accuracies given in these sources.

Table 2.1: Accuracy analysis for four radar altimeters, with an indication of the slope ranges concerned. An absolute bias to the validation data was not supplied for Sentinel-3A. CryoSat-2 is always in SARIn mode over the East Arctic, so only the results for that mode are given.

Mission	Instrument	Product	Comparison data	Accuracy (m)
ERS2 RA	RA	UK PAF	ICESat GLAS	1.12 ±1.16 for surface slope < 0.1°
EnviSat RA2	RA2	SGDRv1	ICESat GLAS	-0.40 ±0.98 for surface slope < 0.1°
Cryo-Sat-2	SIRAL in SARIn mode	L2I baseline C	IceBridge ATM	-0.9 ±1.05 (for a range of slopes, including coastal areas)
Sentinel-3A	SRAL	SR_2_LAN_NT Baseline 2.67	IceBridge ATM and RLA	±0.1 for low slopes in the ice sheet interior, 65-85% of measurements < ±1.0 at the margins

A major cause of differences between the measured and validation data is the surface topography within the beam-limited altimeter footprint, which is compared to a single validation point. There can also be offsets due to snowpack penetration and instrument calibration. The standard deviation of the differences between altimeter and validation data gives a measure of instrument noise and also reflects the different sampling of a rough surface by the two measurement techniques.

For elevation change measurement the precision, i.e. repeatability, of the measurements is more important than the absolute accuracy, as the same technique is used throughout. Precision is gauged by comparing measurements at the crossover points of ascending and descending passes by the same instrument. Over a short time period, typically the cycle time of a mission (approximately 30 days), the actual elevation will vary very little, so differences at the crossovers are mainly due to the measurement precision. During processing, a slope correction is applied to the radar data, and in strongly sloping regions the precision of the correction dominates the measurement error. Thus, some analyses include a term for the slope in their precision statements.

Table 2.2 gives the results of the precision analysis over land ice for ERS-1/2, EnviSat and CryoSat-2 from Schröder et al (2019) and for Sentinel-3A/B from the Sentinel-3 Annual Performance Report 2020 by Raynal and Jettou (2021). These two sources used very different reporting methodologies, the former quoting figures per slope band, the latter concentrating on performance in percentage bands at low slope.

Table 2.2: Precision analysis for the six radar altimeters. In four cases the slope-dependent precision was fitted to a model, and for these the equation is given, where s is the slope in degrees. CryoSat-2 is always in SARIn mode over the East Arctic, so only the results for that mode are given.

Mission	Instrument	Product	Precision (m)
ERS1 RA	RA	Reaper	$0.36 + 2.37s^2$
ERS2 RA	RA	Reaper	$0.38 + 2.57s^2$
EnviSat RA2	RA2	SGDRv2.1	$0.17 + 1.03s^2$
CryoSat-2	SIRAL in SARIn mode	L2I baseline C	$0.38 + 2.01s^2$
Sentinel-3A	SRAL	SR_2_LAN_NT Baseline 2.67	0.1 on slopes $< 0.1^\circ$, up to > 0.3 on the highest slopes
Sentinel-3B	SRAL	SR_2_LAN_NT Baseline 1.41	0.1 on slopes $< 0.1^\circ$, up to > 0.3 on the highest slopes

Further information is available from the quality control websites for each mission;

- ERS 1/2: <http://reaper.mssl.ucl.ac.uk/qa/index.html>
- EnviSat: <http://ra2qa.mssl.ucl.ac.uk/cgi-bin/main.pl>
- CryoSat-2: <http://cryosat.mssl.ucl.ac.uk/qa/>
- Sentinel-3 A/B: <https://sentinels.copernicus.eu/web/sentinel/technical-guides/sentinel-3-altimetry/data-quality-reports>

3. Use Case II (HMA)

3.1 Introduction

This section describes the accuracy assessment and validation of products generated for Use Case 2 (High Mountain Asia). The products include glacier length changes and change rates derived from optical satellite sensors, ice velocity maps and time series of glacier velocity derived from both optical and Synthetic Aperture Radar (SAR) missions, as well as elevation changes derived from optical altimetry and DEM differencing. The products cover the ongoing surges of three glaciers in the central Karakoram, mostly over the period 2000 to 2021. The glaciers are the North and South Chongtar Glacier and a small unnamed glacier referred to as NN9. Included are optical (Sentinel-2, Landsat, Planet) and synthetic aperture radar (SAR) imaging sensors (Sentinel-1, TerraSAR-X), altimeter data from ICESat-2 and DEMs from the Shuttle Radar Topography Mission (SRTM), the Satellite Pour l'Observation de la Terre (SPOT), the High Mountain Asia DEM (HMA-DEM) and DEMs from the Advanced Spaceborne Thermal Emission and reflectance Radiometer (ASTER) by Hugonnet et al. (2021).

3.2 Validation and Intercomparison

3.2.1 Length changes and advance rates

The uncertainty of the length change data has been determined by measuring for each glacier and each time step different points at the terminus. From the range of values, a reasonable mean length change value was determined manually. As sensors with different spatial resolutions are used (e.g. Landsat MSS, ETM+, OLI and Sentinel-2), the uncertainty varies with the sensor, i.e. 60 m for MSS, 30 m for TM, 15 m for OLI pan and 10 m for Sentinel-2 for an assumed one pixel uncertainty. As frontal advances have only been measured for a change of at least 3 to 4 pixels, the measured values should be outside the uncertainty range in most cases. However, the frontal advance rates of the two smaller glaciers show fluctuations that can likely be attributed to measurement uncertainties. In reality, the increase of advance rates over time might have been smoother and more gradual (see <https://doi.org/10.5194/tc-2021-370> for images).

3.2.2 Velocity from optical and SAR

3.2.2.1 *Stable terrain differences*

Based on the assumption that measurement errors over glaciers and other terrain are common (Paul et al. 2017), we assessed the uncertainties of glacier flow velocities from stable terrain velocity observations. We used the same stable area as used for DEM co-registration and derived measures of median and a robust standard deviation based on the median of absolute differences (MAD) which is less sensitive to outliers (e.g. Dehecq et al. 2015).

The displacements measured by Landsat over the selected stable areas show median values close to the expected value of zero, with a MAD between 0.01 and 0.04 m d⁻¹, as reported in (see Table 3.1). Among the Landsat data, Landsat 7 shows the smallest standard deviation based on the MAD. For Sentinel-2, the uncertainties of the displacement on stable terrain are

lower for the pairs with a time interval of approximately a year. For these pairs, the median and the MAD of the velocity are of the same order of magnitude as the Landsat results. For shorter time intervals (5 to 45 days), the Sentinel-2 velocity shows median values from 0.15 to 1.58 m d⁻¹ with a maximum MAD of 1.39 m d⁻¹. Displacement from Planet data gives the largest error with median and MAD values ranging from 0.3 m d⁻¹ to 2.50 m d⁻¹. One pair showed a significantly higher error with a median value of 8.64 m d⁻¹ and a corresponding MAD value of 4.76 m d⁻¹, which is in a similar order of magnitude as the displacement measured in the centre line of the glacier (13.89 m d⁻¹). TerraSAR-X (TSX) revealed the lowest uncertainty with values of both median and MAD approximately zero.

Analysis of measured offsets in stable terrain was performed for all velocity data sets derived from TSX and is described in detail in the Product Validation and Intercomparison Report of the Glaciers_cci project (Glaciers_cci-D4.1_PVIR, 2017). The outcome of the stable ground test showed on average a mean of -0.01 m d⁻¹ and 0.00 m d⁻¹ and an RMSE of 0.05 m d⁻¹ and 0.06 m d⁻¹ for the easting and northing components, respectively (see Table 3.1).

Table 3.1: Overview of the Landsat-7, Landsat-8, TSX, Sentinel-2 and Planet satellite image pair used for flow velocity analysis together with the estimated velocity uncertainty on stable terrain and the maximum velocity along the flowline.

No of pairs	Sensor	Start date (YYYY/MM/D)	End date (YYYY/MM/D)	Time interval (day)	Velocity stable terrain		Velocity flowline		
					Median (m d ⁻¹)	MAD (m d ⁻¹)	NN09 (m d ⁻¹)	North C. (m d ⁻¹)	South C. (m d ⁻¹)
1	L7	2000/09/04	2002/08/04	699	0.01	0.01	0.30	0.14	0.14
2	L8	2013/07/30	2014/07/01	336	0.01	0.06	0.62	0.63	0.23
3	L8	2014/07/01	2015/07/04	368	0.01	0.06	0.76	0.54	0.23
4	L8	2015/07/04	2016/09/24	448	0.01	0.09	0.50	0.53	0.25
5	L8	2016/09/24	2017/10/29	400	0.01	0.04	0.42	0.45	0.36
6	L8	2018/07/12	2019/07/31	384	0.02	0.04	0.75	0.46	0.40
7	TSX	2011/11/12	2011/12/04	22	0.00	0.00	0.10	0.35	0.24
8	TSX	2012/09/09	2012/11/25	77	0.00	0.01	0.11	0.36	0.27
9	TSX	2014/04/10	2014/05/24	44	0.01	0.01	0.08	0.24	0.25
10	S2	2016/11/14	2017/11/04	355	0.04	0.01	0.22	0.27	0.30
11	S2	2107/07/27	2018/08/06	375	0.02	0.01	0.24	0.28	0.31
12	S2	2018/08/06	2019/08/06	365	0.03	0.01	0.35	0.30	0.40
13	S2	2019/08/06	2019/09/25	50	0.07	0.04	0.48	0.90	0.91
14	S2	2019/09/25	2020/08/25	335	0.01	0.01	0.44	0.90	-
15	S2	2020/08/25	2020/10/09	45	0.17	0.04	0.83	1.05	-
16	S2	2019/09/25	2020/06/21	270	0.02	0.12	-	-	1.15
17	S2	2020/06/21	2020/07/11	20	0.21	0.19	-	-	4.38
18	S2	2020/07/11	2020/08/25	45	0.15	0.29	-	-	16.62
19	S2	2020/08/25	2020/08/30	5	1.58	0.34	-	-	25.68
20	S2	2020/08/30	2020/09/19	20	0.09	0.22	-	-	26.77
21	S2	2020/09/19	2020/09/24	5	1.52	0.51	-	-	25.32
22	S2	2020/09/24	2020/10/04	10	0.40	0.48	-	-	24.52
23	S2	2020/10/04	2020/10/09	5	1.25	0.28	-	-	26.25
24	S2	2020/10/09	2020/10/19	10	0.40	0.11	-	-	24.05
25	S2	2020/10/19	2020/11/03	15	0.53	0.37	-	-	16.64
26	S2	2020/11/03	2020/11/08	5	1.03	0.38	-	-	14.85
27	S2	2020/11/08	2020/12/03	25	0.54	1.39	-	-	12.30
28	S2	2020/12/03	2020/12/18	15	0.18	0.14	-	-	10.00

29	S2	2020/12/18	2021/01/02	15	0.30	0.09	-	-	9.49
30	S2	2021/01/02	2021/01/12	10	0.65	0.17	-	-	8.54
31	S2	2021/01/12	2021/01/27	15	0.28	0.16	-	-	8.87
32	S2	2021/01/27	2021/02/16	20	0.17	0.24	-	-	8.13
33	S2	2021/02/16	2021/04/27	70	0.08	0.63	-	-	6.70
34	S2	2021/04/27	2021/05/02	8	1.67	0.24	-	-	8.17
35	PL	2020/06/23	2020/06/30	7	0.35	0.33	-	-	4.62
36	PL	2020/06/30	2020/07/04	4	0.89	0.70	-	-	5.51
37	PL	2020/07/04	2020/07/14	10	0.51	0.57	-	-	5.48
38	PL	2020/07/14	2020/07/20	6	1.27	2.30	-	-	8.43
39	PL	2020/07/20	2020/07/30	10	8.64	4.76	-	-	13.89
40	PL	2020/07/30	2020/08/08	9	0.40	0.58	-	-	17.79
41	PL	2020/08/08	2020/08/16	8	0.32	0.26	-	-	15.15
42	PL	2020/08/16	2020/08/24	8	0.49	0.31	-	-	22.20
43	PL	2020/08/24	2020/09/01	8	1.24	3.07	-	-	23.32
44	PL	2020/10/05	2020/10/08	3	2.51	1.42	-	-	30.81
45	PL	2020/10/08	2020/10/11	3	1.75	0.87	-	-	26.87
46	PL	2020/10/11	2020/10/15	4	1.71	1.42	-	-	27.99
47	PL	2020/10/15	2020/10/18	3	0.34	1.69	-	-	26.13

3.2.2.2 Dataset intercomparison (L8 vs. TSX, S2 vs. L8, Planet & S1)

The sensor intercomparison revealed a very good agreement between the velocity data derived from TerraSAR-X and Landsat 8, Sentinel-2 and Planet, as well as Landsat 8 and Sentinel-2 (Figure 3.1). Velocity values along the flowline derived from the 15 m resolution Landsat 8 panchromatic band for the period July 2018 to July 2019 are the same as from 10 m resolution Sentinel-2 data for the period August 2018 to August 2019. The average difference between the Landsat and Sentinel-2 velocity is about 0.00047 m d^{-1} , with an uncertainty of 0.027 m d^{-1} (one standard deviation). The Planet images cover only the lower part of the glacier. Here, the Planet velocity reveal the same increase/decrease pattern of the Sentinel-2 velocity profile. Direct comparison of flow velocities reveals only small differences that can be related to slightly different time intervals. The high-resolution TerraSAR-X sensor revealed by far the best results, also depicting the flow fields of the two smaller glaciers precisely (Figure 3.2).

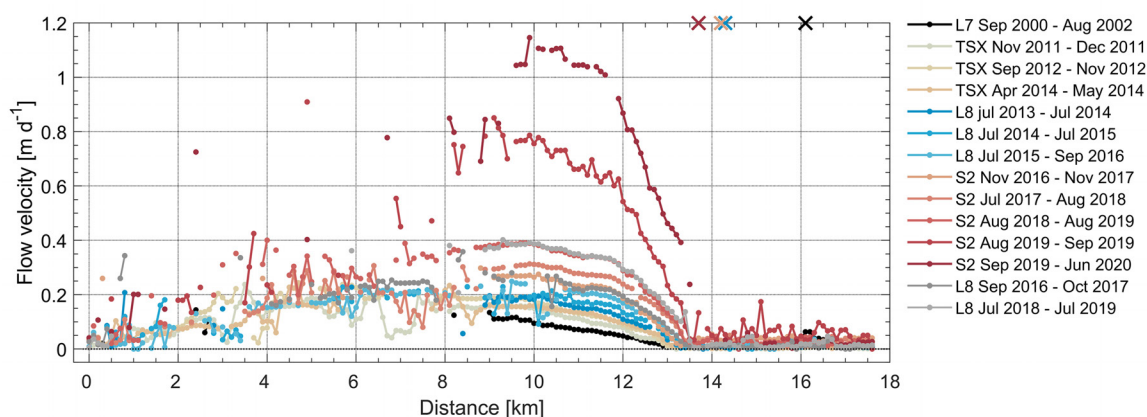


Figure 3.1: Temporal evolution of flow velocities for South Chongtar Glacier. Pre-surge values along the centre-line from Landsat (L7, L8), TerraSAR-X (TSX), and Sentinel-2 (S2)

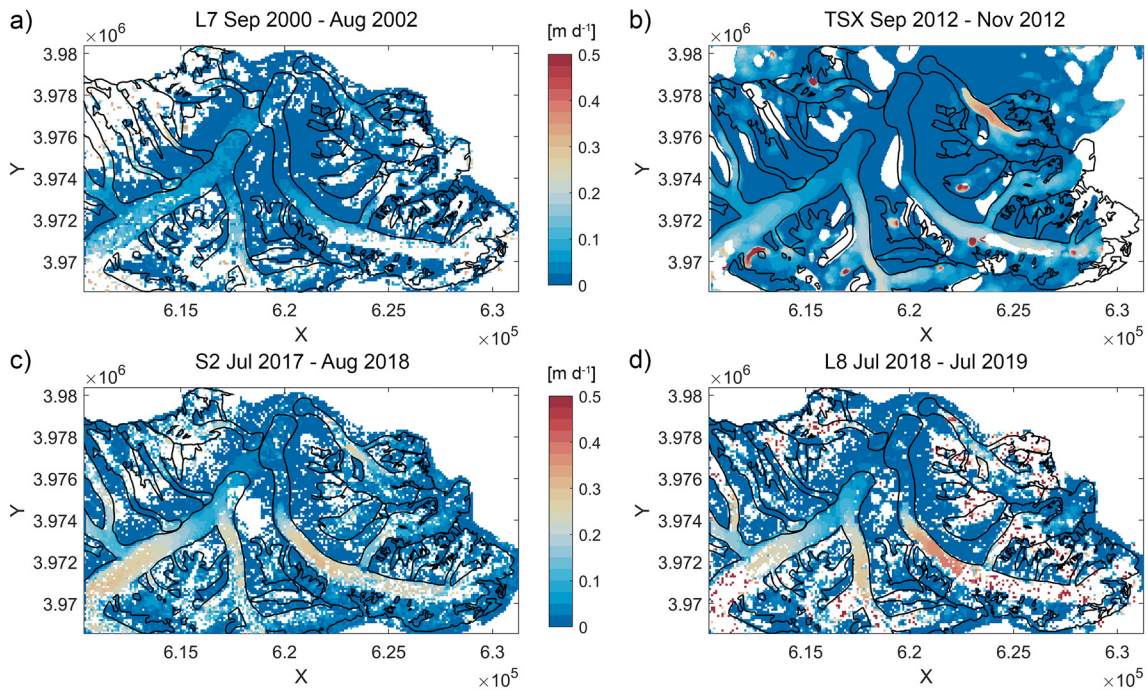


Figure 3.2: Temporal evolution of 2D surface flow velocities for the three glaciers before 2020 derived from a) Landsat 7, b) TSX, c) Sentinel-2, and d) Landsat 8. The dates of the compared images are given at the top of each panel.

3.2.2.3 Dataset intercomparison: Sentinel-1 versus Sentinel-2

Chongtar Glacier

Radar satellites can ‘see’ through clouds and Sentinel-1 offers frequent and systematic coverage in areas prone to monsoon clouds as the Himalayas. Despite radar speckle and 74 m x 56 m spatial resolution of 20x4 multi-looked products, the rapid advance of Chongtar glacier since July 2020 can be clearly observed in Sentinel-1 backscattering intensity images (Figure 3.3). The animation of 12-days S-1 backscattering intensity images can be employed to exemplarily show the sudden advance of Chongtar glacier since Summer 2020 (Paul et al., subm.).

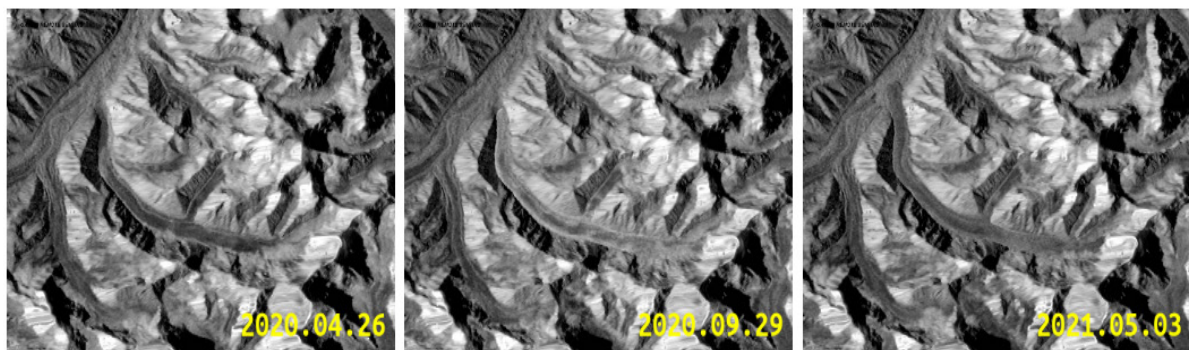


Figure 3.3: Sentinel-1 multi-looked backscattering intensity images of South Chongtar Glacier for (a) 2020.04.26, (b) 2020.09.29 and (c) 2021.05.03.

SAR offset tracking requires relatively large image templates of around 64-512 pixels for cross-correlation to compensate for radar speckle (Strozzi et al., 2002; Paul et al., 2015; Leinss and Bernard, 2021). The pixel spacing of S-1 IW data is ~ 2.3 m in slant-range (~ 3.5 m in ground-range for an incidence angle of 40 degrees) and ~ 14 m in azimuth. Chongtar Glacier is a relatively long glacier with a length of more than 18 km in April 2021, but it is quite narrow with a width generally smaller than 800 m. The glacier is generally east-west oriented in its upper part, bending towards south-north in its lower quarter. Tests with various image template sizes were performed with the S-1 image pair of 04.11.2020-16.11.2020 at the peak of the surge (Figure 3.4). The best trade-off between signal and noise is visually found for an image template size of 128x64 pixels.

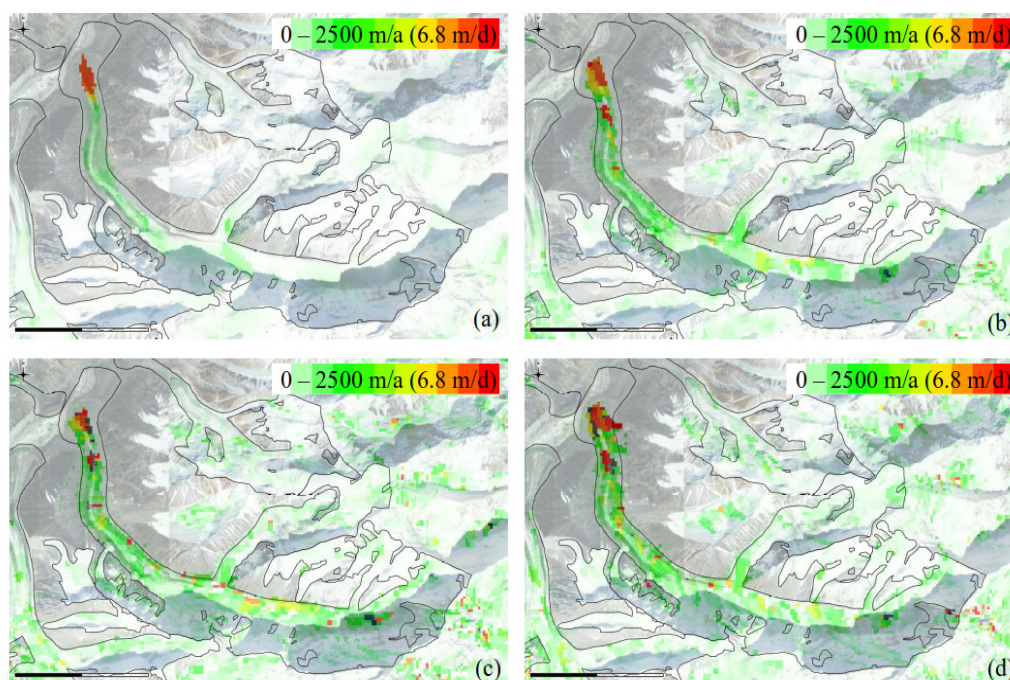


Figure 3.4: Ice surface velocity of Chongtar Glacier from Sentinel-1 data of 04.11.2020-16.11.2020 for different image template sizes: (a) 256 x 128 (900m x 1800m), (b) 128 x 64 (450m x 900m), (c) 128 x 32 (450m x 450m) and (d) 64 x 64 (225m x 900m).

Orthorectified S-2 data were tracked with the Gamma software using a template size of 32x32 pixels (i.e. 320 m x 320 m). No filter was applied in post-processing to the offsets. A visual comparison of the ice surface velocity maps determined from S-1 and S-2 for two periods is shown in Figure 3.5, while the comparison along a central flow line of the glacier is presented in Figure 3.6. The large image template sizes of 128 x 64 (450 m x 900 m) for Chongtar glacier (width < 800 m) result in a strong underestimation of the S-1 ice surface velocities with errors much larger than those indicated in previous studies for larger Arctic glaciers (Paul et al., 2017; Strozzi et al., 2017).

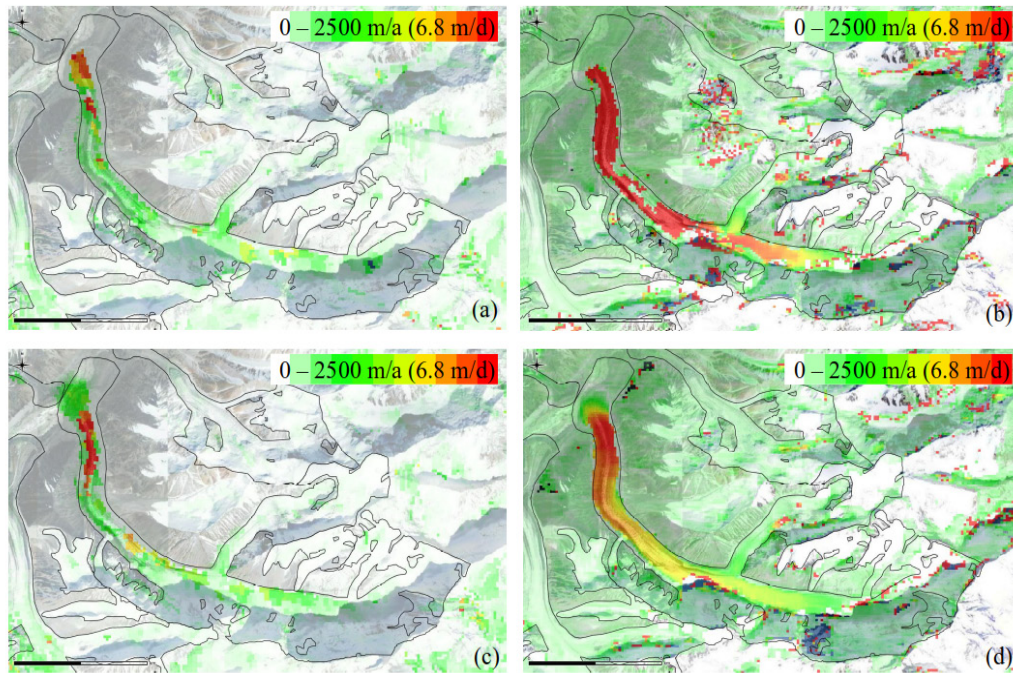


Figure 3.5: Ice surface velocity of Chongtar Glacier from (a) Sentinel-1 data of 04.11.2020-16.11.2020, (b) Sentinel-2 data of 03.11.2020-08.11.2020, (c) Sentinel-1 data of 08.02.2021-20.02.2021, (d) Sentinel-2 data of 11.02.2021-16.02.2021.

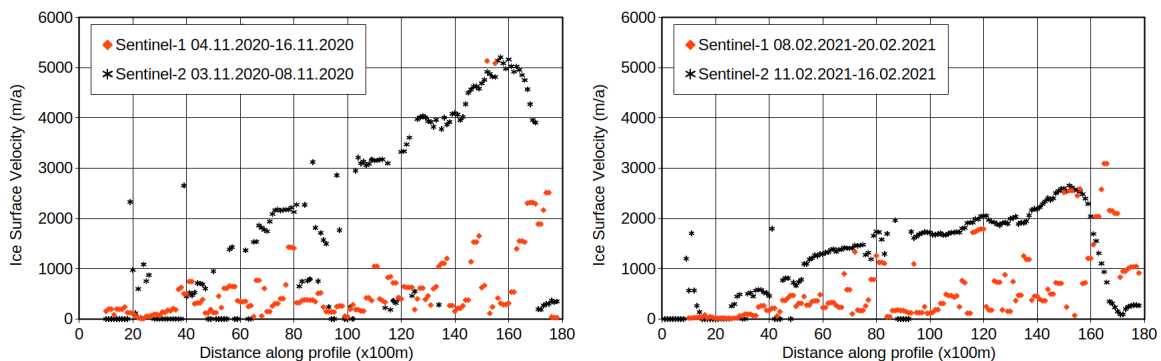


Figure 3.6: Ice surface velocity on a profile along a centre-line of South Chongtar Glacier from Sentinel-1 and Sentinel-2 data.

The comparison between S-1 and S-2 along the centre-line of South Chongtar Glacier indicates that around distance 150 (x100 m) there is a somehow better agreement. This area corresponds to the region where the glacier exits the relatively narrow Chongtar Valley to enter the larger Sarpo Lago valley. The time-series of S-1 velocity around this position is shown in Figure 3.7.

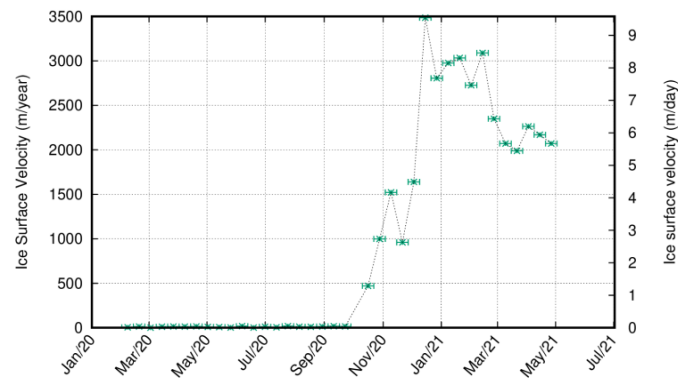


Figure 3.7: Time-series of Sentinel-1 velocity around distance 150 (x100 m) along the centre-line of Chongtar Glacier.

CN5Y641H0074 West Kunlun Glacier

The surging trunk of CN5Y641H0074 West Kunlun Glacier has a length of about 8 km and a width of about 1.5 km and is flowing first towards north and then bending towards east. In Figure 3.8 we compare Sentinel-1 and Sentinel-2 results in March 2021 and April 2021. The coverage with valid information from S-1 is larger in April 2021 than in March 2021, when strong underestimation of ice surface velocities is observed in the centre of the glacier. The quality of the S-2 results is better in March 2021 than in April 2021, when the glacier and surrounding areas were snow-covered.

The comparison of S-1 and S-2 velocities along the centre line of the glacier is presented in Figure 3.9. For the 46 coincident measurement points in March 2021, the standard deviation of the velocity difference is 55 m/a, while average, minimum, and maximum of the velocity difference are 28 m/a, -122 m/a, and 156 m/a, respectively. For the 60 coincident measurement points in April 2021, the standard deviation of the velocity difference is 60 m/a, while average, minimum, and maximum of the velocity difference are 73 m/a, -68 m/a, and 171 m/a, respectively. A generally good agreement between S-1 and S-2 can be observed around position 80 (x80m) along the centre line of the surging trunk of CN5Y641H0074 West Kunlun Glacier. The time-series of Sentinel-1 velocity around this position is shown in Figure 3.10.

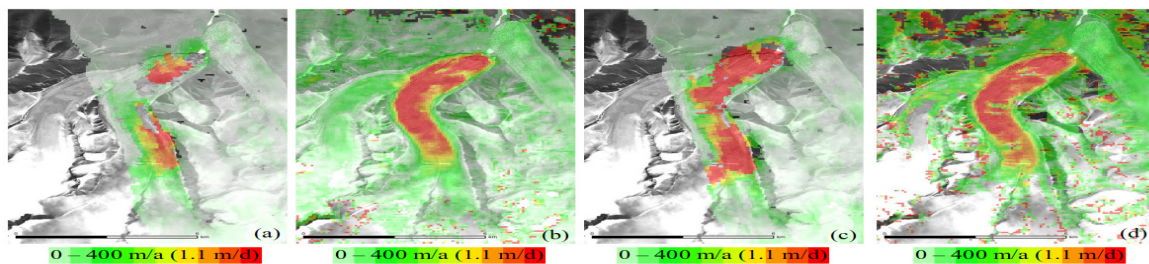


Figure 3.8: Ice surface velocity of the surging trunk of CN5Y641H0074 West Kunlun Glacier from Sentinel-1 and Sentinel-2 data: (a) Sentinel-1 13.03.2021-25.03.2021, (b) Sentinel-2 10.03.2021-20.03.2021, (c) Sentinel-1 06.04.2021-18.04.2021, (d) Sentinel-2 16.04.2021-26.04.2021.

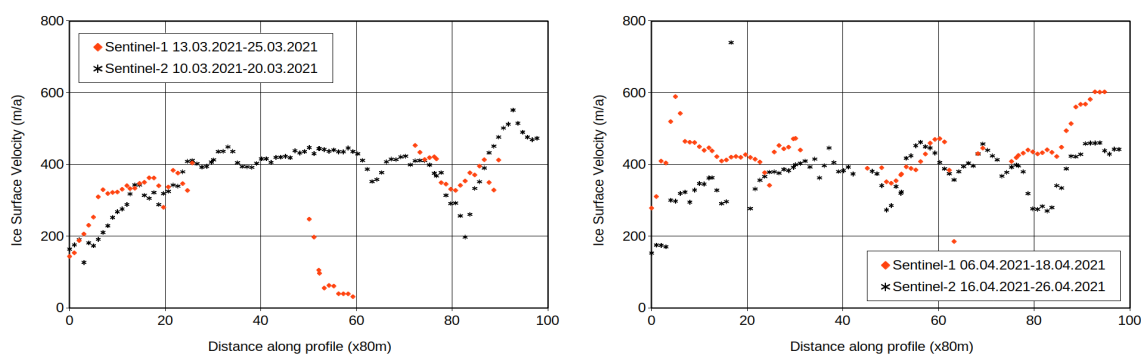


Figure 3.9: Ice surface velocity on a profile along the centre line of the surging trunk of CN5Y641H0074 West Kunlun Glacier from Sentinel-1 and Sentinel-2 data.

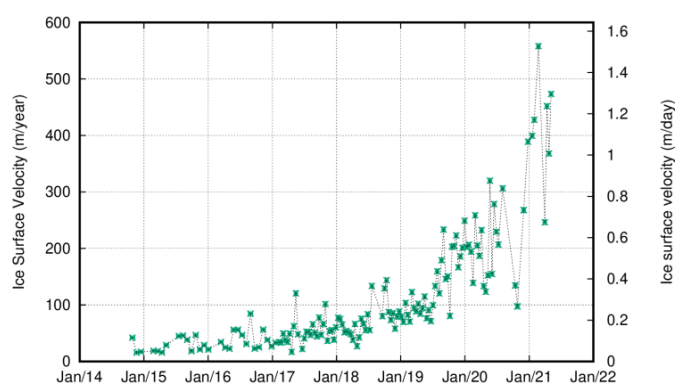


Figure 3.10: Time-series of Sentinel-1 velocity around distance 80 (x100m) along the centre flow-line of the surging trunk of CN5Y641H0074 West Kunlun Glacier.

Rimo Glacier

The main trunk of Rimo Glacier has a length of about 15 km and a width of more than 2 km and is flowing towards east. In Figure 3.11 we compare S-1 and S-2 results in July 2019 and July 2020. In both cases it is evident the effect of the different resolutions and image template sizes used for tracking between S-1 and S-2, with the latter showing better detailed displacement fields. The comparison of S-1 and S-2 velocities along the centre line of the glacier is presented in Figure 3.12. In general, there is a good agreement between S-1 and S-2 along the whole centre line of Rimo Glacier. For the 131 coincident measurement points in July 2019, the standard deviation of the velocity difference is 357 m/a, while average, minimum, and maximum of the velocity difference are 44 m/a, -2160 m/a, and 735 m/a, respectively. It has to be noted that Rimo Glacier was in July 2019 at the peak of its surge, with very large velocities and an extremely high spatial and temporal variability of ice surface velocity, making it inappropriate for precise validation. The additional profiles of S-2 velocities for June and September 2019 in Figure 3.12. clearly show the extraordinary dynamic of this glacier in the summer of 2019. For the 151 coincident measurement points in July 2020, the standard deviation of the velocity difference is 37 m/a, while average, minimum, and maximum of the velocity difference are 35 m/a, -82 m/a, and 127 m/a, respectively.

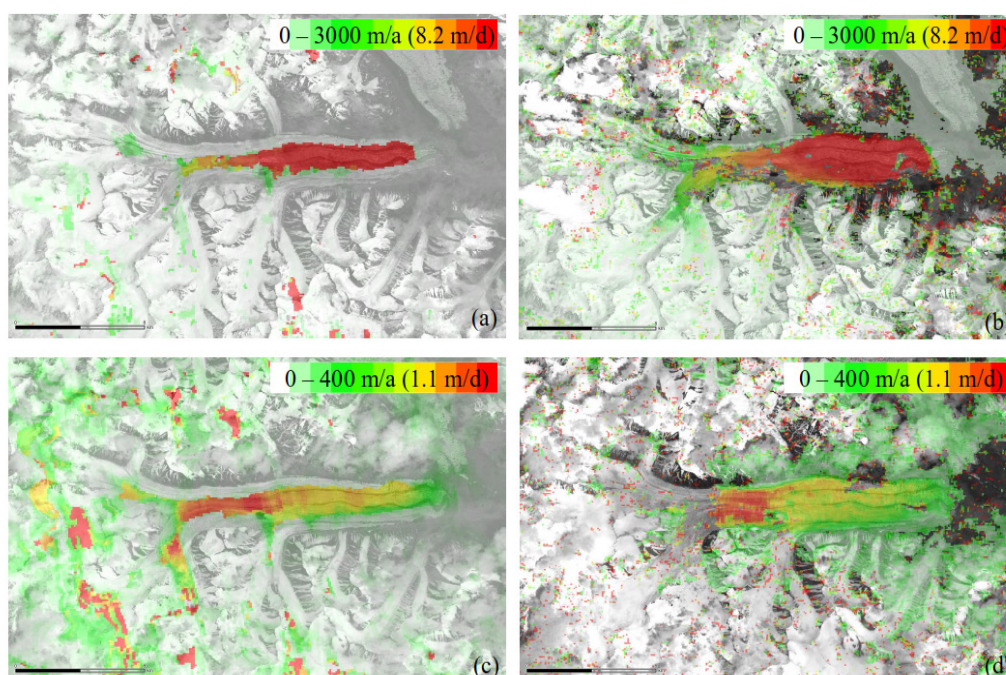


Figure 3.11: Ice surface velocity of Rimo Glacier from Sentinel-1 and Sentinel-2 data: (a) Sentinel-1 20.07.2019-01.08.2019, (b) Sentinel-2 24.07.2019-08.08.2019, (c) Sentinel-1 14.07.2020-26.07.2020 and (d) Sentinel-2 13.07.2020-28.07.2020.

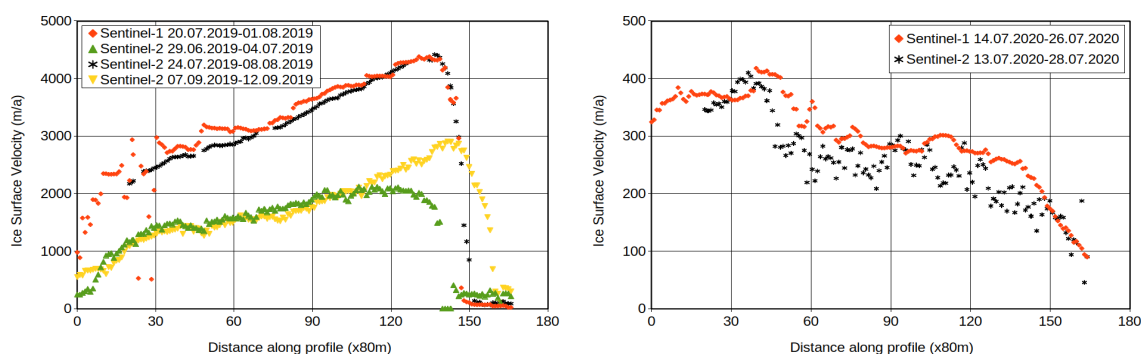


Figure 3.12: Ice surface velocity on a profile along the centre flow-line of Rimo Glacier from Sentinel-1 and Sentinel-2 data.

Final remarks

Chongtar Glacier, the surging trunk of CN5Y641H0074 West Kunlun Glacier and the main trunk of Rimo Glacier are relatively long glaciers (18 km, 8 km and 15 km, respectively), but they have different widths. Chongtar Glacier is relatively narrow, with a width generally smaller than 800 m, and the ice surface velocities estimated from Sentinel-1 are nearly everywhere strongly underestimated. The surging trunk of CN5Y641H0074 West Kunlun Glacier is larger than Chongtar Glacier, with a width of about 1.5 km. The underestimation of ice surface velocities is observed only in some areas during certain periods. The comparison with S-2 ice surface velocities for two image pairs in March 2021 and April 2021 indicates that standard deviations of the velocity difference are 55 m/a and 60 m/a, respectively. The main trunk of Rimo Glacier has a width of more than 2 km and in general we observe a good agreement between S-1 and S-2 along the whole centre line of Rimo Glacier. The standard

deviation of the velocity difference between S-1 and S-2 in July 2020 is 37 m/a, a value similar to previously published estimates for large Arctic glaciers by Strozzi et al. (2017), i.e. between ± 20 and ± 30 m/a for 12-day S-1 data in areas far from relatively small glacier calving fronts and shear zones. We conclude that the minimum width of a glacier to be reliably observed with Sentinel-1 in the Himalayas is around 2 km. For a width of about 1 to 2 km there might be so some limited areas with a reliable estimate. For a width smaller than 1 km the ice surface velocity estimated from Sentinel-1 are largely wrong.

Sentinel-2 results show more detailed displacement fields than S-1 as a consequence of the smaller image template sizes that can be used for tracking. However, because of the presence of clouds, only S-1 offers the opportunity of a continuous, all-year around monitoring of ice surface velocity every 12 days. The comparison between the S-1 and S-2 ice surface velocities for the investigated glaciers also indicates that there are often areas where S-1 results have a better quality. Time-series of S-1 velocity should therefore be extracted from carefully selected locations to achieve best quality information on the temporal dynamic of ice surface velocity over a surging glacier.

3.2.3 Elevation change

3.2.3.1 Co-registration and DEM accuracy

We analysed 7 DEMs/elevation datasets (Table 3.2). The pre-processing of the DEMs follows the standard processing steps for DEM differencing. All DEMs were projected to UTM 43N (EPSG 32643), and their elevation data were vertically transformed to the WGS 84 ellipsoid. We did not fill voids to avoid introducing uncertainty and errors from interpolation, but rather masked out these areas for further analyses. This removes large parts of the accumulation areas in the case of the SPOT 2010 and 2015 DEMs. The DEMs were resampled, clipped and aligned to the same snap raster with cell size 30 m. The DEMs were co-registered using OPALS (Pfeifer et al., 2014). Specifically, we applied least squares matching to estimate the full 3D affine transformation parameters that minimize the errors with respect to the reference DEM (HMA DEM) over common stable areas. We used the HMA DEM as a reference DEM due to its superior spatial resolution and accuracy on stable terrain (off-glacier) compared to the other DEMs.

Table 3.2: Co-registration accuracy analysis over selected stable terrain areas (off-glacier, slope <40 deg).

Name	Type	Resolution	Date	Source	Comments
SRTM 2000	SAR	1 arcsec (~30 m)	Feb. 2000	USGS, doi:10.5066/f7pr7tft	C Band with penetration
HMA-DEM	OPT	8 m	Feb-Aug 2015	NSIDC, doi:10.5067/KXOVQ9L172S2	7-months composite
SPOT 2010	OPT	30 m	Jan 2010	Gardelle et al. (2013)	SPOT 5-HRS
SPOT 2015	OPT	30 m	Oct 2015	Berthier and Brun (2019)	SPOT 6
SPOT 2020	OPT	10 m	Oct. 2020	Ordered	SPOT 6
ASTER	OPT	30 m	2000-2020	Hugonnet et al. (2021)	5y elevation change
ICESat-2 ATL03	laser	0.7m / >3km	2018-2021	Neumann et al. (2021), doi:10.5067/ATLAS/ATL03.004	ATL03 individual photon elevation data
ICESat-2 ATL06	laser	40m / >3km	2018-2021	Smith et al. (2021), doi:10.5067/ATLAS/ATL06.004	ATL06 elevation profiles

Stable areas were manually identified outside the glacier and slope values larger than 40 degrees were excluded from the mask of stable areas. Therefore, co-registration accuracy of the DEMs was computed from elevation differences calculated over stable terrain (Table 3.3). For ICESat-2 data, we used the AMES stereo pipeline (version 2.7.0, Shean et al., 2016) to co-register the elevation profiles (only off-glacier samples) with the already co-registered DEMs, and found no co-registration offset. The spatially sparse ICESat-2 profiles do not cover the selected stable areas very well and are thus not included in the comparison in Table 3.3.

Table 3.3: Co-registration accuracy analysis over selected stable terrain areas (off-glacier, slope <40 deg).

Datasets	Mean	Std	Median	Min	Max
HMA DEM 2015 – SPOT 2010 (30m)	1.3234	9.8660	1.0303	-104.01	379.3369
HMA DEM 2015 – SPOT 2015 (30m)	0.5066	13.2438	-0.1199	-51.09	423.1772
HMA DEM 2015 – SRTM 2000 (30m)	0.6316	9.3655	1.0229	-113.01	154.4829
SPOT 2020 – HMA DEM 2015 (5m)	1.2817	3.0735	1.0840	-176.69	61.5708
<i>SPOT 2010 – SRTM 2000 (30m)</i>	<i>-0.5831</i>	<i>11.4501</i>	<i>-0.3081</i>	<i>-365.42</i>	<i>143.2505</i>
<i>SPOT 2015 – SPOT 2010 (30m)</i>	<i>0.7842</i>	<i>15.8529</i>	<i>1.2217</i>	<i>-424.44</i>	<i>118.0737</i>
<i>SPOT 2020 – SRTM 2000 (30m)</i>	<i>2.3728</i>	<i>8.7969</i>	<i>2.5359</i>	<i>-103.09</i>	<i>59.3291</i>
<i>SPOT 2020 – SRTM 2000 (5m)</i>	<i>3.0963</i>	<i>11.0475</i>	<i>3.4722</i>	<i>-257.99</i>	<i>101.4824</i>

ICESat-2 ATL06 elevation uncertainties are derived from the sum in quadrature of the expected RMS segment misfit and the vertical geolocation error. ATL03 elevation uncertainties of individual photons are in the order of decimetres on the relatively smooth glacier surface.

From a visual inspection of the elevation differences, we found no indication of remaining horizontal shifts between the DEMs after the co-registration. The median elevation differences to the reference DEM (HMA DEM) are 1.02 m (SRTM), 1.03 m (SPOT 2010), -0.12 m (SPOT 2015) and 1.08 m (SPOT 2020), with standard deviations of 3-15 m. Also mean elevation differences, which are more sensitive to extreme values, are <1.4 m for all DEM difference pairs except for the SPOT 2020-SRTM2000 DEM pair (2.4 ±8.8 m). These are small elevation errors within the range of expected uncertainties also after successful co-registration, considering the extremely steep and rugged terrain. The mean uncertainty of the ICESat-2 ATL06 data was ±5.37 m.

3.2.3.2 Dataset intercomparison: SPOT2015 vs HMA DEM

The comparison of the SPOT October 2015 and HMA 2015 (spring composite) DEMs shows a minor tiling effect caused by the composite nature of the HMA DEM in the upper accumulation areas of North and South Chongtar Glacier. The slight advance of North Chongtar and surge reservoir build-up on South Chongtar within the few months' time gap are visible (blue areas on the tongues). The rising elevations of the South Chongtar tongue are also visible in the tongue cross transects in the middle panels in Figure 3.13 (bright red/orange data points). In contrast, the elevations of the two DEMs agree very well in the top and bottom panels in that figure, corresponding to transects in the upper accumulation area and the down-wasting tongue in the main valley. Apart from artefacts and local differences in very steep terrain, elevation values of the HMA DEM and the SPOT DEM from 2015 thus agree very well both on the glacier tongues and outside (stable area statistics in Table 3.3).

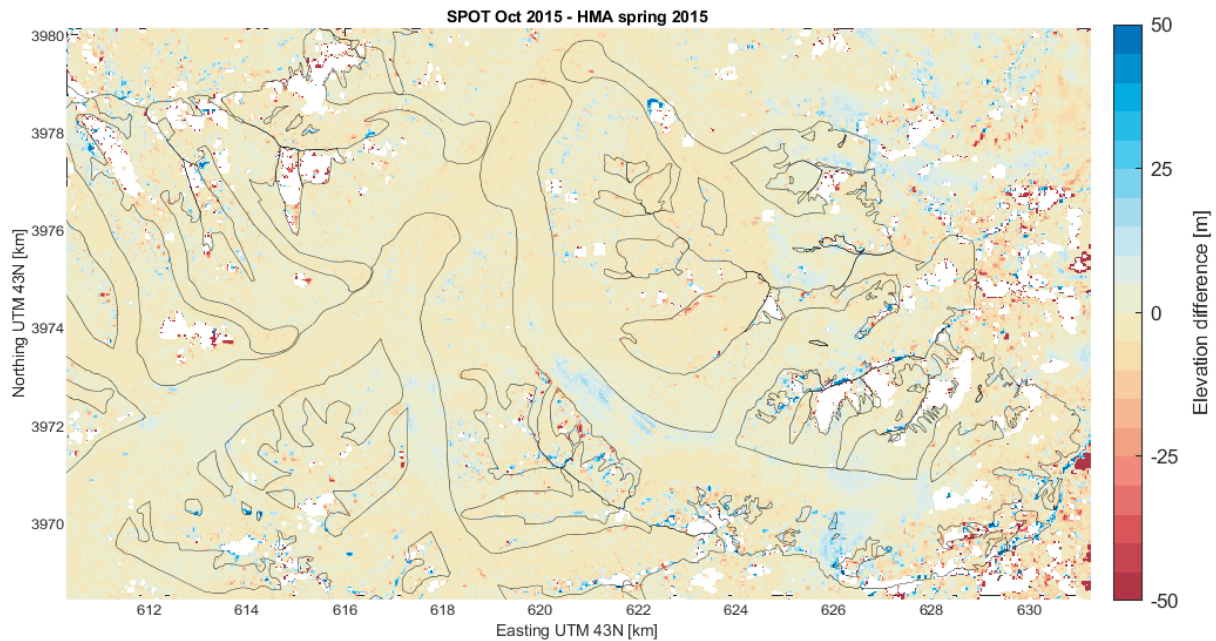


Figure 3.13: The comparison of two DEMs acquired within a few months in 2015 shows very good agreement except for artefacts in very steep areas, which are to be expected.

3.2.3.3 Dataset intercomparison: SPOT/SRTM vs. ASTER

The elevation change values derived from the ASTER DEM time series by Hugonnet et al. (2021) agree with the time series we analysed from SRTM, SPOT and the HMA DEMs (Figure 3.14). The SPOT/SRTM DEM difference images reveal more artefacts and local differences especially in very steep terrain. Data voids and artefacts are located elsewhere in the ASTER data, and it has a spatial filter applied, resulting in a smoother background in off glacier-areas and to some degree also the glacier areas. Locally the information is less complete, e.g., the advance of North Chongtar is not well covered, and the surge advance of the glacier NN8 is not visible (both areas marked with black arrows in Figure 3.14). For small areas or narrow glacier tongues, the ASTER DEM time series thus contain less information compared to DEMs specifically generated or processed for our study region.

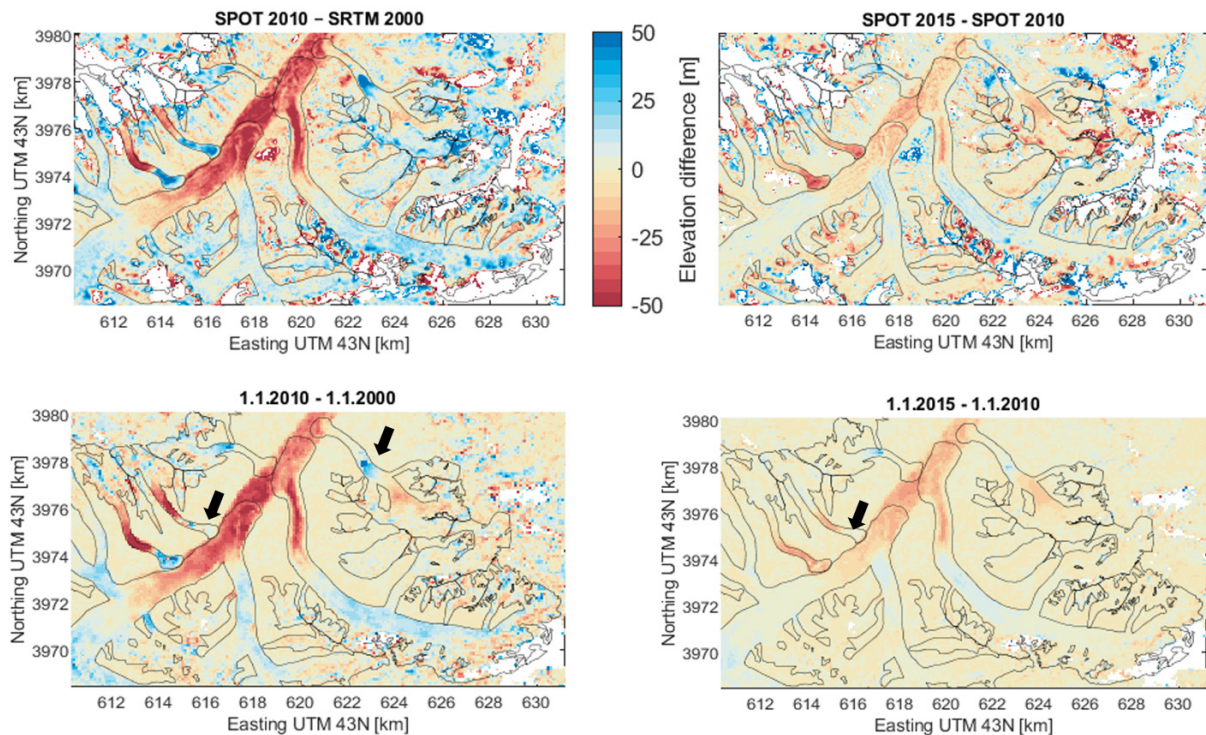


Figure 3.14: Comparison of elevation changes from different DEM products for the same time span. Upper panels: DEMs co-registered within this study, lower panels: ASTER DEM differences from Hugonnet et al. (2021). The ASTER DEM difference product does not resolve surges of narrow glacier tongues equally well (black arrows).

3.2.3.4 Dataset intercomparison: ICESat-2 vs. DEMs

Figure 3.15 shows a comparison of all available elevation values along the ground tracks of one ICESat-2 overpass from December 2019. ICESat-2 photon data surpasses all other DEMs in terms of elevation accuracy and precision, and reveals most detail of the glacier surface, including crevasses/rugged surfaces (bottom right panel). ICESat-2 has three beam pairs, each consisting of a weak and a strong beam separated only 90m in distance. In the bright, snow-covered accumulation area, both the weak (left panels) and strong beams (right panels) provide equally good data. On the tongue, and in particular the downwasting main glacier tongue in the valley with a darker and more rugged surface, ICESat-2's weak beam yields considerably fewer photon returns, resulting in a poor representation of the surface compared to the strong beam of the same beam pair.

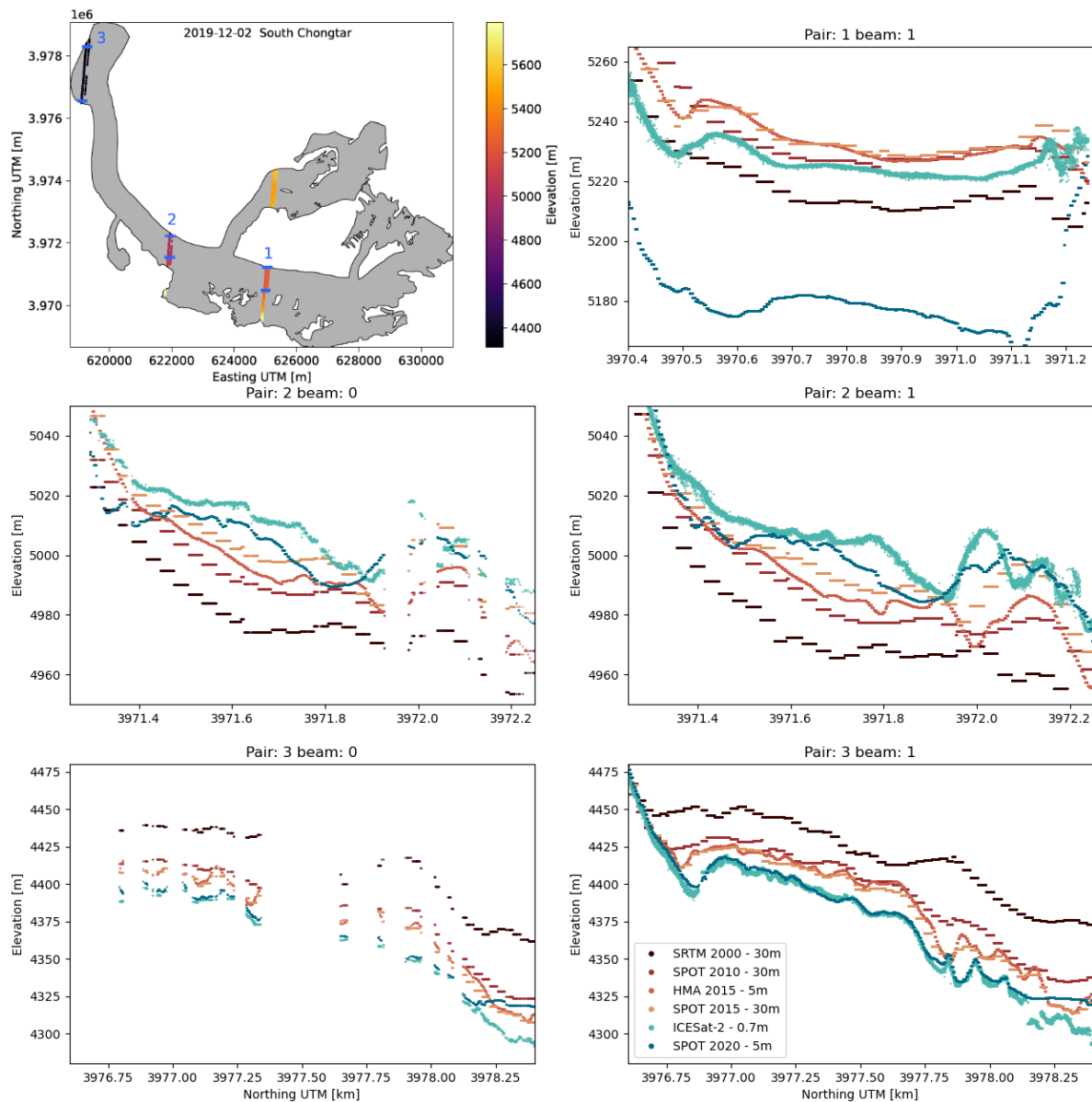


Figure 3.15: Cross-transsects along five of the six profiles of the ICESat-2 overpass of 2. December 2019 (overview map on top left panel). The panels on the left show ICESat-2's weak beams, the ones on the right the right beams of each the three beam pairs. Corresponding DEM elevations for each photon identified as a glacier surface return (cyan) are shown in colours ordered by DEM acquisition date (red to blue, legend in bottom right panel).



4. References

- Berthier, E. and Brun, F.: Karakoram geodetic glacier mass balances between 2008 and 2016: persistence of the anomaly and influence of a large rock avalanche on Siachen Glacier, *J. Glaciol.*, 65, 494–507, 2, 2019.
- Brenner, A., DiMarzio, J. and Zwally, H.: Precision and Accuracy of Satellite Radar and Laser Altimeter Data Over the Continental Ice Sheets, *IEEE T. Geosci. Remote*, 45, 321–331, 2007.
- Dowdeswell J., T. Benham, T Strozzi and J.O. Hagen: Iceberg calving flux and mass balance of the Austfonna ice cap on Nordaustlandet, Svalbard, *Journal of Geophysical Research*, 133, F03022, doi:10.1029/2008JF000905, 2008.
- Gardelle, J., Berthier, E., Arnaud, Y., and Käab, A.: Region-wide glacier mass balances over the Pamir-Karakoram-Himalaya during 1999–2011, *The Cryosphere*, 7, 1263–1286, 2013.
- Hugonnet, R., McNabb, R., Berthier, E., Menounos, B., Nuth, C., Girod, L., Farinotti, D., Huss, M., Dussaillant, I., Brun, F., and Käab, A.: Accelerated global glacier mass loss in the early twenty-first century, *Nature*, 592, 726–731, 2021.
- Leclercq, P. W., Käab, A., and Altena, B.: Brief communication: Detection of glacier surge activity using cloud computing of Sentinel-1 radar data, *The Cryosphere*, 15, 4901–4907, 2021.
- Leinss, S. and P. Bernard TanDEM-X: Deriving InSAR Height Changes and Velocity Dynamics of Great Aletsch Glacier, *IEEE Journal of Selected Topics of Applied Earth Observation and Remote Sensing*, accepted for publication.
- Li, S., S. Leinss and I. Hajnsek, Cross-Correlation Stacking for Robust Offset Tracking using SAR Image Time-Series, *IEEE Journal of Selected Topics in Applied Earth Observations and Remote Sensing*, PP (99):1-1, doi:10.1109/JSTARS.2021.3072240, 2021.
- McMillan, M., Muir, A., Shepherd, A., Escolà, R., Roca, M., Aublanc, J., Thibaut, P., Restano, M., Ambrozio, A., and Benveniste, J. (2019): Sentinel-3 Delay-Doppler altimetry over Antarctica, *The Cryosphere*, 13, 709–722, 2019.
- Neumann, T. A., A. Brenner, D. Hancock, J. Robbins, J. Saba, K. Harbeck, A. Gibbons, J. Lee, S. B. Luthcke, T. Rebold, et al. 2021. ATLAS/ICESat-2 L2A Global Geolocated Photon Data, Version 4. Boulder, Colorado USA. NASA National Snow and Ice Data Center Distributed Active Archive Center. <https://doi.org/10.5067/ATLAS/ATL03.004>. [Last accessed 16 October 2021].
- Nilsson, J., Gardner, A., Sandberg Sørensen, L., and Forsberg, R.: Improved retrieval of land ice topography from CryoSat-2 data and its impact for volume-change estimation of the Greenland Ice Sheet, *The Cryosphere*, 10, 2953–2969, 2016.
- Nuth, C., Gilbert, A., Köhler, A., McNabb, R., Schellenberger, T., Sevestre, H., Weidle, C., Girod, L., Luckman, A., and Käab, A.: Dynamic vulnerability revealed in the collapse of an Arctic tidewater glacier, *Scientific Reports*, 9, 5541, <https://doi.org/10.1038/s41598-019-41117-0>, 2019.
- Paul, F., T. Bolch, A. Käab, T. Nagler, C. Nuth, K. Scharrer, A. Shepherd, T. Strozzi, F. Ticconi, R. Bhambri, E. Berthier, S. Bevan, N. Gourmelen, T. Heid, S. Jeong, M. Kunz, T.R. Lauknes, A. Luckman, J. Merryman, G. Moholdt, A. Muir, J. Neelmeijer, M. Rankl, J. Van Looy and T. Van Niel, The glaciers climate change initiative: Methods for creating glacier area, elevation change and velocity products, *Remote Sensing of Environment*, 162: 408–426, 2015.

- Paul, F., T. Bolch, K. Briggs, A. Käab, M. McMillan, R. McNabb, T. Nagler, C. Nuth, P. Rastner, T. Strozzi and J. Wuite, Error sources and guidelines for quality assessment of glacier area, elevation change, and velocity products derived from satellite data in the Glaciers_cci project, *Remote Sensing of Environment*, 203: 256-275, 2017.
- Pfeifer, N., Mandlbürger, G., Otepka, J., and Karel, W.: OPALS – A framework for Airborne Laser Scanning data analysis, *Computers, Environment and Urban Systems*, 45, 125–136, 2014.
- Raynal, M. and Jettou, G. (2021): S3MPC STM Annual Performance Report - Year 2020, accessed Nov 2021 (<https://sentinels.copernicus.eu/documents/247904/3519647/Sentinel-STM-Annual-Performance-Report-2020.pdf/2887259c-d168-c0ee-0d5a-5fec11926aba?t=1621611181956>).
- Schröder, L., Horwath, M., Dietrich, R., Helm, V., van den Broeke, M. R., and Ligtenberg, S. R. M. (2019): Four decades of Antarctic surface elevation changes from multi-mission satellite altimetry, *The Cryosphere*, 13, 427–449, 2019.
- Smith, B., Fricker, H. A., Gardner, A., Siegfried, M. R., Adusumilli, S., Csathó, B. M., Holschuh, N., Nilsson, J., Paolo, F.S., and the ICESat-2 Science Team: ATLAS/ICESat-2 L3A Land Ice Height, Version 3, NASA NSIDC Distributed Active Archive Center [dataset], <https://doi.org/10.5067/ATLAS/ATL06.003>, 2020, [last access: 3 December 2020].
- Strozzi, T., A. Luckman, T. Murray, U. Wegmüller, and C. Werner, Glacier motion estimation using SAR offset-tracking procedures, *IEEE Transactions on Geoscience and Remote Sensing*, 40 (11), 2384-2391, 2002.
- Strozzi, T., F. Paul, A. Wiesmann, T. Schellenberger, and A. Käab, Circum-Arctic Changes in the Flow of Glaciers and Ice Caps from Satellite SAR Data between the 1990s and 2017, *Remote Sensing*, 9(9), 947, doi:10.3390/rs9090947, 2017.
- Strozzi, T., Kouraev, A., Wiesmann, A., Wegmüller, U., Sharov, A., and Werner, C.: Estimation of Arctic glacier motion with satellite L-band SAR data, *Remote Sensing of Environment*, 112, 636–645, 2008.
- Strozzi, T., Paul, F., Wiesmann, A., Schellenberger, T., and Käab, A.: Circum-Arctic Changes in the Flow of Glaciers and Ice Caps from Satellite SAR Data between the 1990s and 2017, *Remote Sensing*, 9, 947, 2017.

Acronyms

ADP	Algorithm Development Plan
ALOS	Advanced Land Observing Satellite
ASTER	Advanced Spaceborne Thermal Emission and Reflection Radiometer
ATM	Airborne Topographic Mapper
CC	Correlation Coefficient
CRDP	Climate Research Data Package
DEM	Digital Elevation Model
DGPS	Differential Global Positioning System
ECA	Elevation Change Altimetry
ENVISAT	Environmental Satellite
EO	Earth Observation
ERS	European Remote-Sensing Satellite
ETM+	Enhanced Thematic Mapper plus
FAU	Friedrich-Alexander Universität Erlangen-Nürnberg
GAMDAM	Glacier Area Mapping for Discharge from the Asian Mountains
GLAS	Geoscience Laser Altimeter System
GLIMS	Global Land Ice Measurements from Space
GO	Glacier Outline
GoLIVE	Global Land Ice Velocity Extraction from Landsat 8
GPS	Global Positioning System
GRACE	Gravity Recovery and Climate Experiment
HMA	High Mountain Asia
ICESat	Ice, Cloud, and land Elevation Satellite
ID	Identifier
InSAR	Interferometric SAR
ITS LIVE	Inter-Mission Time Series of Land Ice Velocity and Elevation
IV	Ice Velocity
IW	Interferometric Wide
JERS	Japanese Earth Resources Satellite 1
L8	Landsat 8
MAD	Median of Absolute Differences
MEaSURES	Making Earth System Data Records for Use in Research Environments
NSIDC	National Snow and Ice Data Center
OPALS	Orientation and Processing of Airborne Laser Scanning
OT	Offset Tracking
PALSAR	Phased Array type L-band Synthetic Aperture Radar
PVIR	Product Validation and Intercomparison Report
PVP	Product Validation Plan
QA	Quality Assessment
RA	Radar Altimeter
RADAR	Radio Detection and Ranging
RGI	Randolph Glacier Inventory
RLA	Riegl Laser Altimeter
RSME	Root Mean Square Error
S-1	Sentinel-1



S-2	Sentinel-2
SAR	Synthetic Aperture Radar
SARIn	SAR Interferometry mode
SIRAL	SAR Interferometer Radar Altimeter
SNR	Signal-to-Noise Ratio
SPOT	Satellite Pour l'Observation de la Terre
SRAL	SAR Altimeter
SRTM	Shuttle Radar Topography Mission
STD	Standard Deviation
TSX	TerraSAR-X
UCR	Uncertainty Characterisation Report
URD	User Requirements Document